Applied Catalysis B: Environmental 140–141 (2013) 433–443

Contents lists available at SciVerse ScienceDirect

Applied Catalysis B: Environmental

journal homepage: www.elsevier.com/locate/apcatb

Facile large-scale synthesis of β-Bi_2O_3 nanospheres as a highly efficient photocatalyst for the degradation of acetaminophen under visible light irradiation

Xin Xiao[a], Ruiping Hu[a], Chao Liu[a], Chunlan Xing[a], Cheng Qian[a], Xiaoxi Zuo[a], Junmin Nan[a,b,*], Lishi Wang[b]

[a] School of Chemistry and Environment, South China Normal University; Key Lab of Theoretical Chemistry of Environment, Ministry of Education, Guangzhou 510006, PR China
[b] Key Laboratory of Fuel Cell Technology of Guangdong Province; School of Chemistry and Chemical Engineering, South China University of Technology, Guangzhou 510640, PR China

ARTICLE INFO

Article history:
Received 11 January 2013
Received in revised form 15 April 2013
Accepted 16 April 2013
Available online 24 April 2013

Keywords:
β-Bi_2O_3 nanospheres
Photocatalysis
Visible light
Acetaminophen
Photodegradation mechanism

ABSTRACT

A facile solvothermal–calcining route for the large-scale synthesis of uniform β-Bi_2O_3 nanospheres has been demonstrated. The morphology, structure, and photoabsorption of β-Bi_2O_3 were characterized, and the effects of the preparation conditions on the structural properties of products were analyzed. The results show that monodisperse bismuth nanospheres are formed through the solvothermal reaction where the D-fructose acting as the dominant reductant, and subsequently converted to β-Bi_2O_3 nanospheres after the calcination in air. It is shown that the composition and structure of the products are greatly affected by the amount of D-fructose, the solvothermal and calcination temperature. The formation mechanism of β-Bi_2O_3 nanospheres is assumed to undergo the "in situ reduction" of Bi(III)–ethylene glycol complex spheres which serve as self-sacrificing templates, followed by the "in situ oxidation" of bismuth nanospheres by oxygen during the calcination in air. The visible light-induced photocatalysis of the synthetic photocatalysts applied to the degradation of acetaminophen (APAP, a widely occurring human-derived pharmaceutical found in the environment) has been studied systematically. The photocatalytic reaction of APAP over the β-Bi_2O_3 nanospheres follows pseudo first-order kinetics according to the Langmuir–Hinshelwood model, and exhibits a higher reaction rate constant, which is 2.5, 7, 8.1, and 79 times higher than that of commercial Bi_2O_3, synthetic α-Bi_2O_3, nitrogen doped TiO_2 (N-TiO_2), and Degussa P25, respectively. The superior photocatalytic activity is attributed to the narrower band gap energy (approximately 2.36 eV), nanostructure, good dispersion and high oxidation power of the β-Bi_2O_3 nanospheres. Only one intermediate at *m*/*z* 110 can be detected by liquid chromatography/mass spectrometry (LC/MS) in the photodegradation process, while several low-molecular-weight organic acids were identified by ion chromatography (IC) analysis. By combining with the experimental determination of reactive oxygen species in the photocatalytic process and the theoretical calculation of frontier electron density of APAP, a simple, hole-predominated photodegradation pathway is proposed. In addition, the high mineralization efficiency indicates that the as-synthesized β-Bi_2O_3 nanospheres photocatalyst can avoid secondary pollution during photocatalysis, which is important in practical applications.

1. Introduction

In the past decades, there is a great concern about the presence of pharmaceutical and personal care products (PPCPs) in the aquatic environment, as they, even at small concentrations, might produce chronic toxicity, endocrine disruption and development of pathogen resistance [1–3]. In particular, these products and their metabolites are often not (or only marginally) biodegradable, resulting in an inefficient removal by conventional wastewater treatment plants (WWTPs) [4,5]. Acetaminophen (N-acetyl-*p*-aminophenol, APAP), also known as paracetamol, is used all over the world as an antipyretic and analgesic drug for the relief of mild to moderate pain associated with headache, backache, arthritis and postoperative pain [6]. As a result of this widespread use, APAP has been frequently detected in sewage treatment plant effluents,

* Corresponding author at: School of Chemistry and Environment, South China Normal University; Key Lab of Theoretical Chemistry of Environment, Ministry of Education, Guangzhou 510006, PR China. Tel.: +86 20 39310255; fax: +86 20 39310187.
E-mail address: jmnan@scnu.edu.cn (J. Nan).

0926-3373/$ – see front matter © 2013 Elsevier B.V. All rights reserved.
http://dx.doi.org/10.1016/j.apcatb.2013.04.037

surface water and even drinking water [7]. Overdoses of APAP can lead to the accumulation of toxic metabolites, causing severe and sometimes fatal hepatotoxicity and nephrotoxicity and is in some cases associated with renal failure [8]. In the United States, APAP toxicity has replaced viral hepatitis as the most common cause of acute hepatic failure and is the second most common cause of liver failure requiring transplantation [9]. Therefore, a good knowledge of the fate of APAP during water treatment is urgently required.

So far, researchers have tried to remove APAP from water by various techniques, including physical adsorption [10], enzymatic oxidation [11], UV photodegradation [12], Fenton reaction [13], ozone oxidation [14], electrochemical processing [15], and photocatalytic degradation [16–18]. Among these methods, the heterogeneous photocatalytic technique offers advantages because of its high degradation of APAP and its high mineralization efficiency, low toxicity, low cost, and ability to function under ambient conditions [19,20]. However, although the photocatalytic decomposition of APAP using TiO_2-based photocatalysts with UV light irradiation has been studied extensively [3,16–18,20–22], to the best of our knowledge, the degradation of APAP using a non-titania photocatalyst under visible light irradiation has not been reported. It therefore remains a great challenge to explore new photocatalysts to facilitate the photodegradation of APAP. These new photocatalysts must show high activity, high mineralization efficiency and visible light-driven for efficient utilization of solar light or indoor illumination, and can be used to gain an understanding of the reaction mechanisms for photocatalytic degradation of APAP under visible light irradiation.

As an important multi-functional material, bismuth-containing oxides have many potential applications in photovoltaic cells, non-linear optical glasses, fuel cells, oxygen sensors, and catalysis for selective industrial oxidation reactions due to its excellent properties, such as adjustable band gap, high ion conductivity, and rich polymorphism [23]. To date, many bismuth-containing materials, such as Bi_2O_3 [24,25], $BiVO_4$ [26], Bi_2WO_6 [27], Bi_2MoO_6 [28], $Bi_{12}TiO_{20}$ [29], $Bi_2Fe_4O_9$ [30], Bi_3NbO_7 [31], $NaBiO_3$ [32] and BiOX [33], have been found to be highly active visible light-driven photocatalysts. The good photocatalytic performance of these bismuth oxide-based semiconductors is due partly to the intrinsic polarizability induced by the Bi $6s^2$ lone pair of electrons, favoring the separation of photo-generated electron–hole pairs and the transfer of these charge carriers [34]. Of these compounds, Bi_2O_3 is the simplest and the most significant [35], and it has been suggested that Bi_2O_3 is a suitable photocatalyst owing to its relatively smaller band gap, higher oxidation power of the valence hole, and non-toxic properties [36]. Bi_2O_3 has five polymorphic forms labeled as α-Bi_2O_3 (monoclinic), β-Bi_2O_3 (tetragonal), γ-Bi_2O_3 (body centered cubic), δ-Bi_2O_3 (cubic), and ω-Bi_2O_3 (triclinic) [37]. Among these polymorphic forms, β-Bi_2O_3 has the strongest absorption in the visible light region because it has the smallest band gap (~2.4 eV), and has demonstrated better photocatalytic performance than other phases under visible light irradiation [38]. However, because the beta phase represents a metastable state, the preparation of pure tetragonal Bi_2O_3 is difficult or complicated, especially on the nanoscale [35]. The development of a facile method to produce pure β-Bi_2O_3 with nanostructures for the potential application in visible light photocatalytic treatment of wastewaters is therefore essential.

In this study, we report a facile route to large-scale synthesis of monodisperse β-Bi_2O_3 nanospheres through a solvothermal–calcining process. The morphology, structure, photoabsorption properties, and formation process of the as-synthesized β-Bi_2O_3 nanospheres are systemically investigated, and its photocatalytic activity and mineralization efficiency for APAP degradation are evaluated under visible light irradiation. In addition, the photodegradation intermediates of APAP and the photogenerated reactive species in the system are identified, and a possible photocatalytic degradation mechanism is proposed as well.

2. Experimental

2.1. Materials and methods

Acetaminophen (APAP) was obtained from Aladdin Reagent Co., Ltd. Bismuth nitrate pentahydrate ($Bi(NO_3)_3 \cdot 5H_2O$) was purchased from Tianjin Kermel Chemical Reagent Co., Ltd. Ethylene glycol (EG) was bought from Chinasun Specialty Products Co., Ltd. D-Fructose was purchased from Shanghai Bio Science & Technology Co., Ltd. All of the chemicals were of analytical grade and used as received without further purification.

In a typical synthesis, 1.5 mmol $Bi(NO_3)_3 \cdot 5H_2O$ and 1.5 mmol D-fructose were dissolved completely in 35 mL of EG with magnetic stirring at room temperature. The mixture was then poured into a Teflon-lined stainless-steel autoclave (45 mL capacity) and incubated in an oven at 160 °C for 15 h. After completion of the reaction, the precipitates were collected by centrifugation, washed several times with distilled water and ethanol to remove any ionic residue, and dried in an oven at 60 °C. Finally, the product obtained was calcined in the air at 300 °C for 1 h in a muffle furnace.

For comparison, a N-doped TiO_2 sample was prepared by solvothermal method using ethylenediamine as the nitrogen source according to Yang et al. [39]: 10 mmol tetrabutyl orthotitanate and 30 mL of ethanol were mixed together and stirred for 30 min, and then 1.0 mL of acetic acid was added. After that, 5 mmol ethylenediamine was added dropwise whilst stirring, following added 1.0 mL of deionized water into the mixture, and stirring continued for a further 30 min. Next, the mixed solution was transferred into a Teflon-lined stainless steel autoclave and kept at 120 °C for 20 h. After reaction, the resultant was collected by centrifugation, washing with deionized water and ethanol several times, and then dried at 60 °C overnight. Finally, the product was annealed at 450 °C for 3 h in air to prepare the pale-yellow N-doped TiO_2 sample (Fig. S1, Supporting Information).

2.2. Catalyst characterization

The phase composition of the synthesized samples was characterized by a X-ray diffractometer (XRD, Y2000, Dandong, China) equipped with a Cu Kα X-ray source. The morphology of the samples was determined by an environmental scanning electron microscope (ESEM, FEI Quanta 456 ESEM FEG). The UV–vis diffuse reflection spectra (DRS) were recorded on a UV-vis spectrophotometer (UV-3010, Hitachi, Japan) by using $BaSO_4$ as a reference and were converted from reflection to absorbance by the Kubelka–Munk method. The total organic carbon concentration was measured using an automated total organic carbon analyzer (TOC-V, Shimadzu, Japan).

2.3. Photocatalytic activity measurements

The photocatalytic degradation experiments were performed in a photochemical reactor (XPA-VII, Xujiang, China) equipped with a 1000 W Xe lamp combined with a 420 nm cutoff filter as the light source, and the system was cooled by a circulating water bath maintained at room temperature. All photocatalytic reactions were performed using the same initial conditions: 50 mL APAP solution (10 mg L^{-1}) was mixed with 50 mg catalyst under constant magnetic stirring. Prior to the irradiation, the mixture was stirred for 1 h in the dark to allow the system to reach adsorption equilibrium.

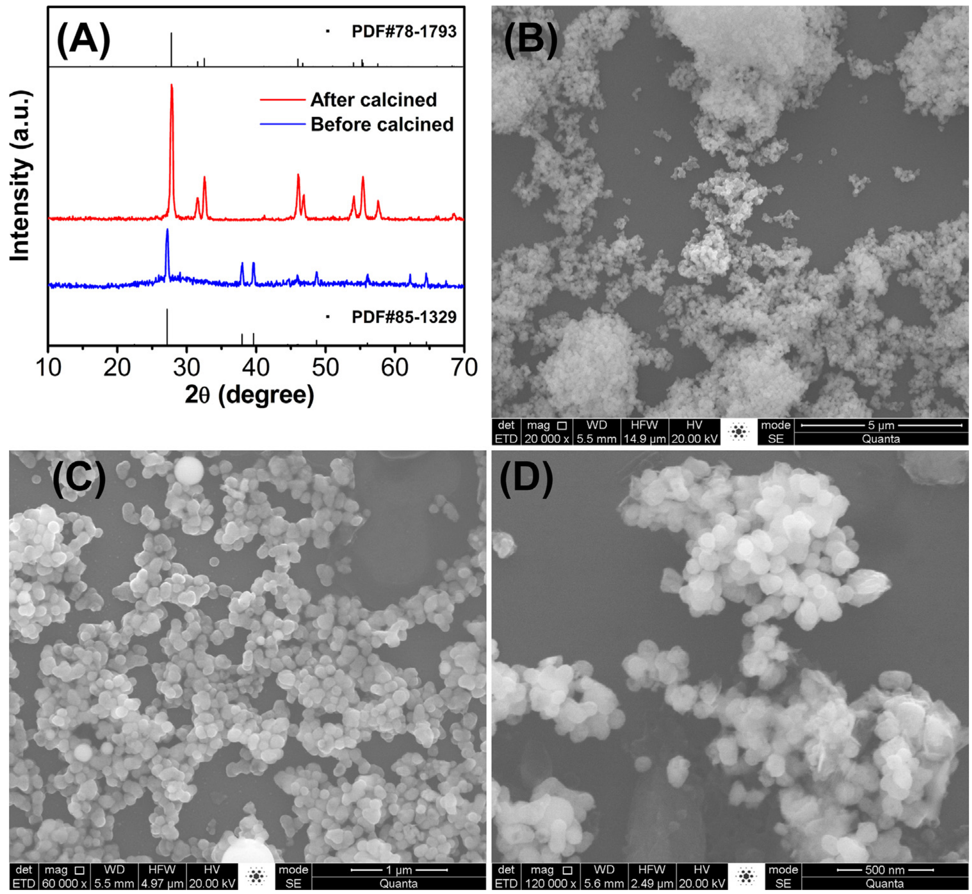

Fig. 1. (A) XRD patterns of the samples before and after calcination at 300 °C for 1 h; (B) low-magnification and (C) high-magnification SEM images of the sample before calcination; (D) high-magnification SEM images of the sample after calcination.

During the photocatalytic process, approximately 2.5 mL of the suspension was taken out, and the solid was subsequently removed from the solution using a 0.45 μm nitrocellulose filter. Afterwards, the APAP content in the solution was determined by UV–vis spectroscopy (UV-1800, Shimadzu, Japan, λ = 242 nm).

2.4. Analysis of the photogeneration intermediates

The photogeneration intermediates in the APAP solution were separated by high-performance liquid chromatography (HPLC, LC-10AT, Shimadzu, Kyoto, Japan) equipped with a UV detector, using a C18 reversed phase column (5 μm, 4.6 mm × 250 mm) at 30 °C with an injection volume of 20 μL. The mobile phase composition was methanol/water (30/70, v/v) at a flow rate of 1 mL min^{-1}. To identify intermediates in the photocatalytic oxidation of APAP, a coupled liquid chromatography/mass spectrometry (LC/MS) equipped with an electrospray ionization source was used and operated in the negative ionization (NI) mode. The selective ion monitoring (SIM) mode with a dwell time of 200 ms and a scan range of 100–250 Da was used to acquire the spectra of APAP and its intermediates. Anionic ozonation products, mainly organic acids, were detected by an ion chromatography (IC, Dionex ICS 900, USA), operated in a recycle mode (ASRS-ULTRA II 4 mm) and equipped with a conductivity detector. Sample injected by an automatic sampler were eluted on a gradient mode at a flow rate of 1.0 mL min^{-1} through an IonPac AS19 analytical column (Dionex, 250 mm × 4 mm) and an IonPac AG19 guard column (Dionex, 50 mm × 4 mm). The ozonation products were then identified based on authentic standard's elution time.

2.5. Quantum chemical calculation

Quantum calculation using Gaussian-09 was carried out to obtain the frontier electronic density (FED) of APAP. Hartree–Fock (HF) theory was chosen for the full optimization of geometries, and 6-31G was used as the basis set of moderate size and accuracy. All optimizations were carried out without any symmetry restrictions and were followed by harmonic frequency analyses to ensure that the optimized conformation was the true global minimum.

3. Results and discussion

3.1. Characterization of β-Bi_2O_3 nanospheres

3.1.1. Morphology and structure

The chemical composition and phase structure of the synthetic samples were confirmed with powder X-ray diffraction (XRD). As shown in Fig. 1A, all diffraction peaks of the sample before and after calcination can be unambiguously assigned to the rhombohedral bismuth (JCPDS No. 85-1329) and tetragonal Bi_2O_3 (JCPDS No. 78-1793), respectively. No impurity peaks are observed, indicating a high purity of the products. Their morphologies and surface structures were then studied by SEM. It can be observed from Fig. 1B and C, before calcination, the sample consists of a large number of monodisperse nanospheres with diameters of ca. 90 nm. And the spherical shapes are maintained after calcination in air at 300 °C (Fig. 1D) although the calcination results in a decrease of their average diameters to ca. 70 nm. The shrinkage maybe ascribed to the structural changes and the evaporation of adsorbed

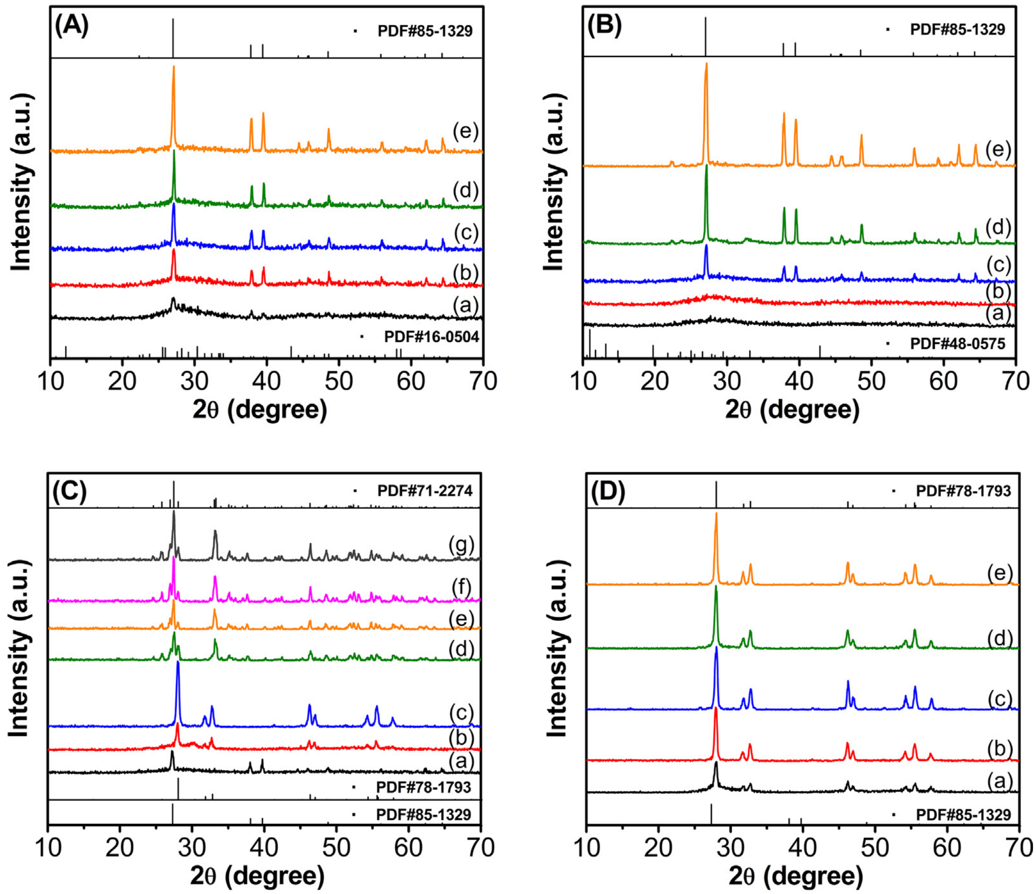

Fig. 2. XRD patterns of the samples (A) before calcination with different amounts of D-fructose: (a) 0 mmol, (b) 1 mmol, (c) 1.5 mmol, (d) 2 mmol, and (e) 3 mmol; (B) before calcination at different solvothermal temperatures: (a) 120 °C, (b) 140 °C, (c) 160 °C, (d) 180 °C, and (e) 200 °C; (C) after calcination at different temperatures: (a) 200 °C, (b) 250 °C, (c) 300 °C, (d) 350 °C, (e) 450 °C, (f) 550 °C, and (g) 750 °C; and (D) after calcination at 300 °C maintained for different times: (a) 0 h, (b) 0.5 h, (c) 1 h, (d) 2 h, and (e) 4 h, respectively.

organics on the nanospheres surface. Combined with the XRD and SEM results, it can be deduced that, under the current route, the metal bismuth nanospheres were formed by solvothermal reaction and then converted completely to β-Bi_2O_3 nanospheres after calcination treatment.

3.1.2. Influence of synthesis conditions

To investigate the influence of preparation conditions on the formation of bismuth (the precursor) and β-Bi_2O_3 nanospheres, four sets of experiments were carried out, varying (i) the amount of D-fructose, (ii) the solvothermal temperature, (iii) the calcination temperature, and (iv) the calcination holding time, while keeping other conditions unchanged. The resulting products were then analyzed by XRD, as shown in Fig. 2.

Fig. 2A shows that the diffraction peaks of the samples synthesized with D-fructose (Fig. 2Ab–e) can be indexed as rhombohedral bismuth and, by increasing the amount of D-fructose, the intensities of the diffraction peaks are enhanced correspondingly. This enhancement can be ascribed to D-fructose as a reducing sugar that can be used as a reducing agent to convert Bi(III) ions to metallic Bi. This is similar to the results previously reported for the preparation of noble metal nanoparticles using D-fructose as reductant [40]. However, without adding D-fructose to the reaction system, the diffraction peaks of the products are fairly low (Fig. 2Aa). In addition to the peaks of bismuth, there are several impurity peaks that can be recognized as bismuth oxide nitrate hydroxide hydrate (JCPDS No. 16-0504). It is well known that ethylene glycol itself can serve as a reductant to prepare metal nanoparticles [41]. However, the reducing ability of ethylene glycol does not seem to be high enough to obtain pure metallic bismuth under the present experimental conditions. Thus, the dominant reductant is D-fructose in this system, while ethylene glycol acts mainly as a high boiling point solvent, stabilizer and coordinating agent to prevent the rapid hydrolysis of $Bi(NO_3)_3$ [42]. Fig. 2B shows the effect of solvothermal temperature on the obtained samples, which clearly indicates that the product with higher crystallinity can be obtained under a higher reaction temperature when the same amount of D-fructose is added. However, when the reaction temperature is too low (<140 °C), the product crystals form in small quantities and with impurities (Fig. 2Ba and Bb), indicating that reaction temperature is another key factor in obtaining a suitable reducing activity for D-fructose. The results may be related to D-fructose is one of the ketone-bearing sugars that require a high temperature to isomerize so that the aldehyde group will be produced in solution, thereby enhancing the reducing ability of D-fructose.

The metallic bismuth nanospheres (reaction at 160 °C with 1.5 mmol D-fructose) were then calcined in air with different calcination temperatures and times. Fig. 2C and D shows that the results are greatly impacted by calcination temperature, but the calcination times have a modest effect. When the temperature is low (200 °C), the phase composition of the sample after the calcining treatment does not change (the sample is still metallic bismuth). After calcination at 250 °C, the sample contains combined phases of β-Bi_2O_3 and metallic bismuth. Whereafter, the diffraction peaks of the sample calcined at 300 °C can be indexed as pure β-Bi_2O_3. The results may be related to the melting point of bismuth is 271 °C.

In the oxygen atmosphere, the metallic bismuth can react with O_2 to form Bi_2O_3 at a temperature higher than the melting point of bismuth. However, if the calcination temperature is higher than 300 °C, the stable phase of bismuth trioxide, i.e., α-Bi_2O_3 (JCPDS No. 71-2274), is produced. The product calcined at 350 °C consists of α-Bi_2O_3 and β-Bi_2O_3 mixed phases, while at higher calcination temperatures (from 450 to 750 °C), the obtained products are pure α-Bi_2O_3. Thus, it is extremely important to control the calcination temperature to produce the pure β-Bi_2O_3.

3.1.3. Possible formation process

To investigate the growth process of the metallic bismuth nanospheres, time-dependent experiments were carefully carried out, and the reaction products were subsequently analyzed by XRD and SEM techniques. The XRD patterns of five typical samples obtained after solvothermal reaction at 160 °C for 1 h, 3 h, 6 h, 9 h and 15 h are shown in Fig. 3A, clearly showing that the characteristic diffraction peaks of metallic bismuth are steadily increasing according to the reaction times. However, it is surprising that although the chemical compositions and structures of the samples are diverse, the SEM images (Fig. 3B–E and Fig. 1C) reveal that all of the samples obtained at different stages have similar nanosphere morphology with approximately identical grain diameter. To find out this secret, the clear solution before solvothermal treatment (inset of Fig. 3F) was observed using an field emission gun environmental scanning electron microscope (ESEM), operating in the environmental: wet mode at low temperature (4 °C) with low water vapor pressure (1000 Pa) [43]. As shown in Fig. 3F, a large number of nanospheres lying at the bottom of the terrarium with a diameter of ca. 100 nm can be clearly observed, which may be ascribed to the formation of Bi(III)–EG complex spheres earlier the solvothermal reaction, as in the previous report of Bi(III)–EG polymer dispersed in ethanol [44]. It is known that Bi(III) exhibits $6s^2$ lone-pair electrons and empty 6p orbitals, which leads it easy to form coordination compounds with variable coordination number [45]. And polyols such as EG can act as complexing agents for several metal ions because of their hydroxyl groups [46]. Accordingly, $Bi(NO_3)_3 \cdot 5H_2O$ can be dissolved in EG or other polyol to form a uniform glycolate complexes solution (Eq. (1)), which constrains systems to prevent precipitation of Bi^{3+}. And these complexes tended to form more highly condensed compounds by intermolecular interactions, which led to a high-molecular-weight network polymer in the system (Eq. (2)) [47]. By this complex-polymerization route, Bi(III)–EG complexing polymer is formed and then dispersed in EG solution (sol), which is similarly to the previously reported synthesis of metal oxides in EG-mediated [48–50]. In order to investigate the morphology of the Bi(III)–polyol complexing polymers, $Bi(NO_3)_3 \cdot 5H_2O$ was dissolved in various polyols, including EG, diethylene glycol (DEG), triethylene glycol (TEG), or mannitol, without addition of D-fructose, and then observed by ESEM technique. As is shown in Fig. S2 (Supporting Information), the Bi(III)–polyol complexing polymers are clearly observed, although the morphologies of them are difference with the solvents. In addition, it was also found that the Bi(III)–EG complexing solution was composed of a large number of small nanosheets instead of nanospheres. Therefore, it is proposed that the D-fructose may play another important role in the formation of Bi(III)–EG complex spheres under current system. However, the exact mechanism is not clear now and needs further investigation.

$$Bi(NO_3)_3 \cdot 5H_2O + 3HOCH_2CH_2OH \rightarrow Bi(OCH_2CH_2OH)_3 + 5H_2O + 3HNO_3 \quad (1)$$

$$n\,Bi(OCH_2CH_2OH)_3 \rightarrow \left[-\overset{|}{\underset{|}{Bi}}-OCH_2CH_2O- \right]_n + H_2O \quad (2)$$

Based on the XRD and SEM observations, the formation mechanism of β-Bi_2O_3 nanospheres may be explained by both the "in situ reduction" and the "in situ oxidation" pathways (Scheme 1), in which the EG, D-fructose, and calcination temperature play key roles. In the beginning, EG serves as a solvent and coordinating agent to hinder the hydrolysis of Bi^{3+}, and to produce Bi(III)–EG complexes after $Bi(NO_3)_3$ is dissolved in EG solution. Then the Bi(III)–EG complexes are further condensed and interacted with D-fructose to form spherical complexing polymer and dispersed well in EG solution to form an uniform solution. As an alpha-hydroxy ketone, D-fructose also dissolves well in EG solvent and surrounds the Bi(III)–EG complex. D-Fructose then combines with EG acting as reductants to convert Bi(III) to metallic bismuth gradually under solvothermal reaction conditions at a relatively high temperature. Simultaneously, the Bi(III)–EG complexing spheres serve as self-sacrificing templates. As a result, the monodisperse Bi nanospheres are obtained after solvothermal treatment. By subsequent annealing in the oxygen environment at temperatures higher than the melting point of bismuth, the Bi nanospheres serve again as self-sacrificing templates and react with O_2 to develop bismuth oxides, and the resulting phase distribution depends on the calcination temperature. When the temperature is approximately 300 °C, a high temperature metastable phase (i.e., the pure beta phase of bismuth oxide) is obtained. Due to a reasonably low calcination temperature, the β-Bi_2O_3 obtained keeps the nanosphere morphology with slight changes.

3.1.4. Photoabsorption properties

The energy band structure feature of a semiconductor is considered as a key factor in determining its photocatalytic activity [51]. Fig. 4A shows the UV–vis diffuse reflection spectra (DRS) of the samples calcined at 250 °C, 300 °C, 350 °C, 450 °C, and 550 °C. The maximal absorbance wavelengths of the pure β-Bi_2O_3 (300 °C, Fig. 4Ab) and pure α-Bi_2O_3 (450 °C and 550 °C, Fig. 4Ad and Ae) are ca. 548, 452, and 444 nm, respectively, suggesting their ability to absorb visible light, while the mixed-phase samples (Fig. 4Aa and Ac) present two absorption bands. Correspondingly, they show significant differences in their colors, as shown in inset for Fig. 4A. Then their band gap energy (E_g) was evaluated using the following equation (Eq. (3)) [52]:

$$\alpha(h\nu) = A(h\nu - E_g)^{n/2} \quad (3)$$

where α, ν, E_g and A are the absorption coefficient, light frequency, band gap energy, and a constant, respectively; n is determined by the type of optical transition of the semiconductor. According to the literature [53], the value of n is 1 for Bi_2O_3. The band gap energies (E_g values) of the samples can thus be estimated from a plot of $(\alpha h\nu)^2$ vs. photon energy ($h\nu$) (also shown in the inset of Fig. 4A) to be approximately 2.36 for β-Bi_2O_3 and 2.78 and 2.83 eV for two α-Bi_2O_3 samples, respectively. The E_g values of β-Bi_2O_3 and α-Bi_2O_3 determined in this work are close to the reported in the literature [38]. In addition, the band position of α-Bi_2O_3 and β-Bi_2O_3 was calculated using the empirical formula (Eq. (4)) [54].

$$E_{VB} = X - E^e + 0.5E_g \quad (4)$$

where E_{VB} is the valence band edge potential, X is the electronegativity of the semiconductor that is the geometric mean of the electronegativity of the constituent atoms, E^e is the energy of free electrons on the hydrogen scale (approximately 4.5 eV), E_g is the band gap energy of the semiconductor, and E_{CB} (conductance band edge potential) can be determined by $E_{CB} = E_{VB} - E_g$. The results are shown in Fig. 4B, which clearly shows that both α-Bi_2O_3 and β-Bi_2O_3 have high oxidation power (sufficiently high valence band potential), while the β-Bi_2O_3 has a narrower band gap than that of α-Bi_2O_3, indicating again its stronger photoabsorption of visible

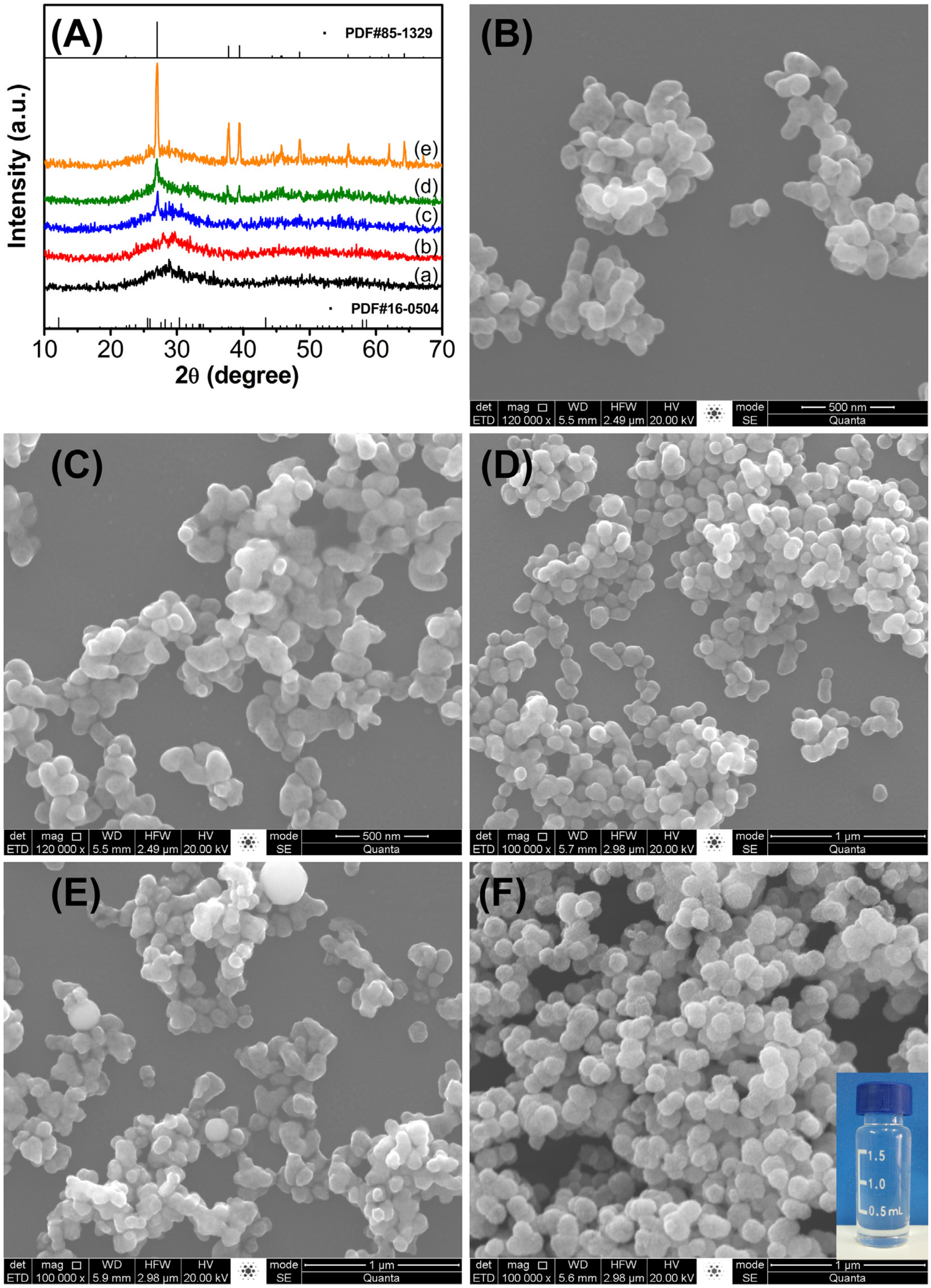

Fig. 3. (A) XRD patterns of the samples after solvothermal reaction for (a) 1 h, (b) 3 h, (c) 6 h, (d) 9 h, and (e) 15 h, respectively; (B–E) SEM images of the samples after solvothermal reaction for (B) 1 h, (C) 3 h, (D) 6 h, and (E) 9 h; (F) ESEM image of the mixture before the solvothermal reaction; the inset shows digital photo of the corresponding sample.

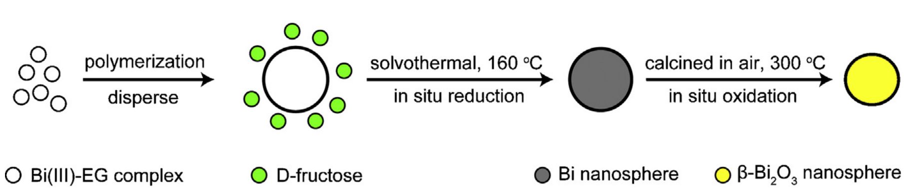

Scheme 1. Illustration of the possible formation process of β-Bi_2O_3 nanospheres.

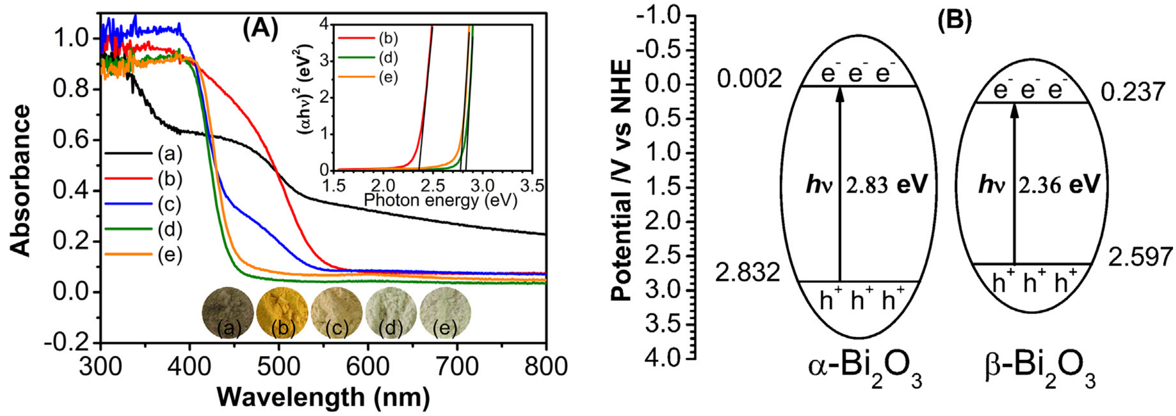

Fig. 4. (A) UV–vis diffuse reflection spectra (DRS) of the samples after calcination at (a) 250 °C, (b) 300 °C, (c) 350 °C, (d) 450 °C, and (e) 550 °C. The inset shows the plots of $(\alpha h\nu)^2$ vs. photon energy ($h\nu$) and the photos of the samples; (B) comparison of the band structures of α-Bi_2O_3 and β-Bi_2O_3. (For interpretation of the references to color in text, the reader is referred to the web version of the article.)

light. The as-synthesized β-Bi_2O_3 sample can thus be predicted to be a satisfying visible light photocatalyst.

3.2. Photocatalytic degradation of acetaminophen

3.2.1. Evaluation of photocatalytic activity and TOC mineralization

The photocatalytic degradation of APAP over the synthesized β-Bi_2O_3 nanospheres was evaluated and compared with the Degussa P25 (a commercially available, highly active, mixed-phase titania photocatalyst), N-doped TiO_2 (synthesized according to the literature [39], with starting N:Ti molar ratios of 1:1), and a commercially available β-Bi_2O_3 sub-microspheres (bought from Aladdin Reagent Co., Ltd., with diameters of ca. 140 nm) under visible light irradiation. It can be seen from Fig. 5A that there is no obvious degradation of APAP using the Degussa P25 as a photocatalyst because it has a large band gap. Under identical irradiation for 180 min, a degradation of 22.8% is observed using the N-doped TiO_2, and the commercial β-Bi_2O_3 results in a degradation of 59.3%, while the removal ratio of 93.6% for APAP can be obtained over the as-synthesized β-Bi_2O_3 nanospheres, showing that the synthetic β-Bi_2O_3 nanospheres have excellent visible light-induced activity. The low activity of the N-TiO_2 is ascribed to its large particle size (Fig. S1B, Supporting Information) and relatively poorer absorption ability in visible light region [39].

The degradation kinetics of APAP using synthetic β-Bi_2O_3 nanospheres, commercial β-Bi_2O_3 sub-microspheres, N-TiO_2, and Degussa P25 were investigated by fitting the experimental data to the Langmuir–Hinshelwood model [55]. Because the reactant concentration was low, the following pseudo first-order kinetics equation (Eq. (5)) was used:

$$-\ln\left(\frac{C_t}{C_0}\right) = k_{app}t \tag{5}$$

where C_0 and C_t are the reactant concentrations at times $t = 0$ and $t = t$, respectively, and k_{app} (min^{-1}) is the apparent reaction rate constant determined by plotting $\ln(C_0/C_t)$ vs. the reaction time (t). The results show that the reaction kinetics of all samples can be very well fitted by the pseudo first-order rate model with high correlation coefficients ($R > 0.995$), as shown in Fig. 5B. The calculated k_{app} values for synthesized β-Bi_2O_3 nanospheres, commercial β-Bi_2O_3 sub-microspheres, N-TiO_2, and Degussa P25 are 0.01387, 0.00543, 0.00172, and 0.0001751 min^{-1}, respectively. Namely, the reaction rate constant of APAP over synthetic β-Bi_2O_3 nanospheres is 2.5, 8.1, and 79 times higher than that of commercial Bi_2O_3, N-TiO_2, and Degussa P25, respectively.

To investigate the influence of calcining temperatures on their photocatalytic activity, the photocatalytic degradation of APAP over the samples annealed at different temperatures and corresponding apparent reaction rate constants was evaluated by using the same method. Fig. 5C and D clearly indicates that the photocatalytic ability of the synthetic samples is affected greatly by their calcination temperature and that all samples are fitted well by the pseudo first-order rate model. The sample calcined at 300 °C (the pure β-Bi_2O_3 nanospheres) achieves the top performance, and the two mixed-phase samples containing β-Bi_2O_3 attain the second and third positions in performance, while the α-Bi_2O_3 samples show poorer activity. The k_{app} values for samples annealing at 200, 250, 300, 350, 450, 550, and 750 °C are calculated to be 0.0001247, 0.00528, 0.01387, 0.00555, 0.00199, 0.00125, 446 and 0.0007413 min^{-1}, respectively, indicating that the reaction rate constant of the β-phase sample is approximately 7–18 times higher than that of the α-phase samples. The superior photoreactivity of the as-synthesized β-Bi_2O_3 nanospheres photocatalyst may be contributed to its narrower band gap energy, nanostructure, good dispersion, high oxidation power, and unique crystal and electronic structures of the beta phase. The decreasing activity of α-Bi_2O_3 samples after heat treatment from 450 °C to 750 °C may be associated with the increase of particle size resulting from the aggregation at higher temperatures.

It is very significant to the effective mineralization of organic compounds throughout the photocatalytic process to avoid secondary pollution in practical applications. Total organic carbon (TOC) was selected as a mineralization index for this system, and the time independence of the TOC data in the APAP solution during the photoreaction is shown in Fig. 6. It can be observed that TOC decreases with time, and after irradiation for 240 min, 89.5% TOC is eliminated, indicating that APAP can be effectively mineralized by using the as-synthesized β-Bi_2O_3 nanospheres as photocatalyst under visible light irradiation.

3.2.2. Analysis of the degradation intermediates and photocatalytic mechanism

To explore the photodegradation products of APAP, the reaction intermediates during the photocatalytic process were detected by LC/MS technique. As shown in Fig. 7A, APAP (m/z 151, Fig. 7C) is eluted at a retention time (RT) of 4.46 min and disappears rapidly, in accordance with UV–vis spectroscopy results. Only one intermediate at m/z 110 was observed at a RT value of 5.51 min. The concentration of this intermediate increased after the photoreaction, reaching its maximum concentration after a reaction time of ca. 30 min, and then quickly decreased until it almost

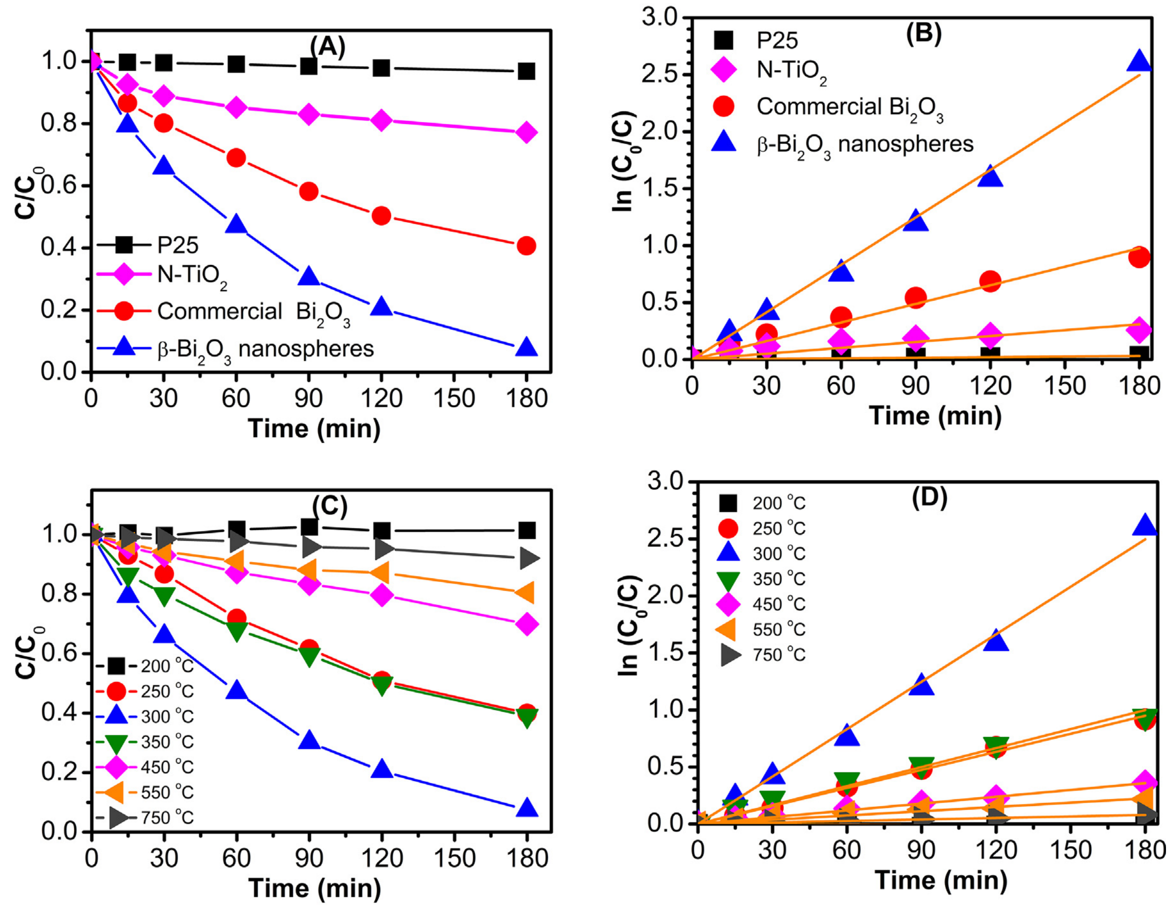

Fig. 5. (A) Photocatalytic degradation kinetics of APAP over β-Bi_2O_3 nanospheres, a commercial Bi_2O_3, N-doped TiO_2, and Degussa P25 under visible light irradiation; (B) Linear plots of $\ln(C_0/C_t)$ vs. degradation time; (C) photocatalytic degradation kinetics of APAP over the Bi_2O_3 samples calcined at different temperatures; and (D) linear plots of $\ln(C_0/C_t)$ vs. degradation time.

disappeared after 180 min (Fig. 7A and B). The results imply that the intermediate was produced during the photodegradation reaction and then was degraded continuously after the subsequent photocatalytic process. The intermediate at RT = 5.51 min is identified as hydroquinone (m/z 110, Fig. 7D), according to the earlier literatures [7,16,21]. In addition, the organic carboxylic acids intermediates generated during the degradation process were analyzed by IC and identified by comparison with commercial standards [56]. It was found that a small amount of hydroxy-acetic acid, formic acid, and succinic acid were detected after the photodegradation for 180 min, which is in agreement with the previous observation in literatures [17,21] and can give an explanation for the TOC residual.

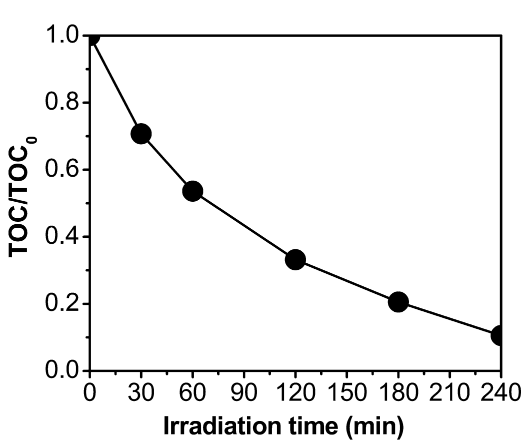

Fig. 6. TOC removal efficiencies of APAP over the as-synthesized β-Bi_2O_3 nanospheres under visible light irradiation.

Many reports on the photocatalytic degradation of APAP over TiO_2 have suggested that the degradation pathways proceed mainly through hydroxylation of APAP because of the formation of reactive hydroxyl radical (•OH) as the most dominant reactant [16,21]. However, in this visible light-induced β-Bi_2O_3 photocatalytic system, no hydroxylated compounds were identified. This observation may be ascribed to the lower standard redox potential of Bi^{5+}/Bi^{3+} (E^0 = 1.59 V at pH 0) compared with the standard redox potential of $^{\bullet}OH/OH^-$ (E^0 = 1.99 V at pH 0). Therefore, holes that were photogenerated on the surface of the photocatalyst could not react with OH^-/H_2O to form •OH [33]. To evaluate the role of primary reactive species, the scavenger experiments were carried out by adding individual scavenger to the photodegradation system. The scavengers used in this study were isopropanol for •OH, sodium oxalate for h^+, 4-hydroxy-2,2,6,6-tetramethylpiperidinyloxy (TEMPOL) for $^{\bullet}O_2^-$, and N_2 for dissolved oxygen [57,58]. As shown in Fig. 8A, with the addition of isopropanol, the photodegradation efficiency remained almost the same as no scavenger added, indicating the •OH was not important in this photocatalytic process. However, significant inhibition effect of photocatalytic performance was observed when sodium oxalate was used to quench h^+, which confirms the important role of h^+ in the photo-oxidation process. In addition, the photodegradation activity of APAP declined to some extent after TEMPOL or N_2 was added, implying that the $^{\bullet}O_2^-$ also plays a role in the system. Hence, the APAP photodegradation over the as-synthesized β-Bi_2O_3 nanospheres may be dominated by the direct hole oxidation rather than the oxidation by •OH. Besides, the dissolved

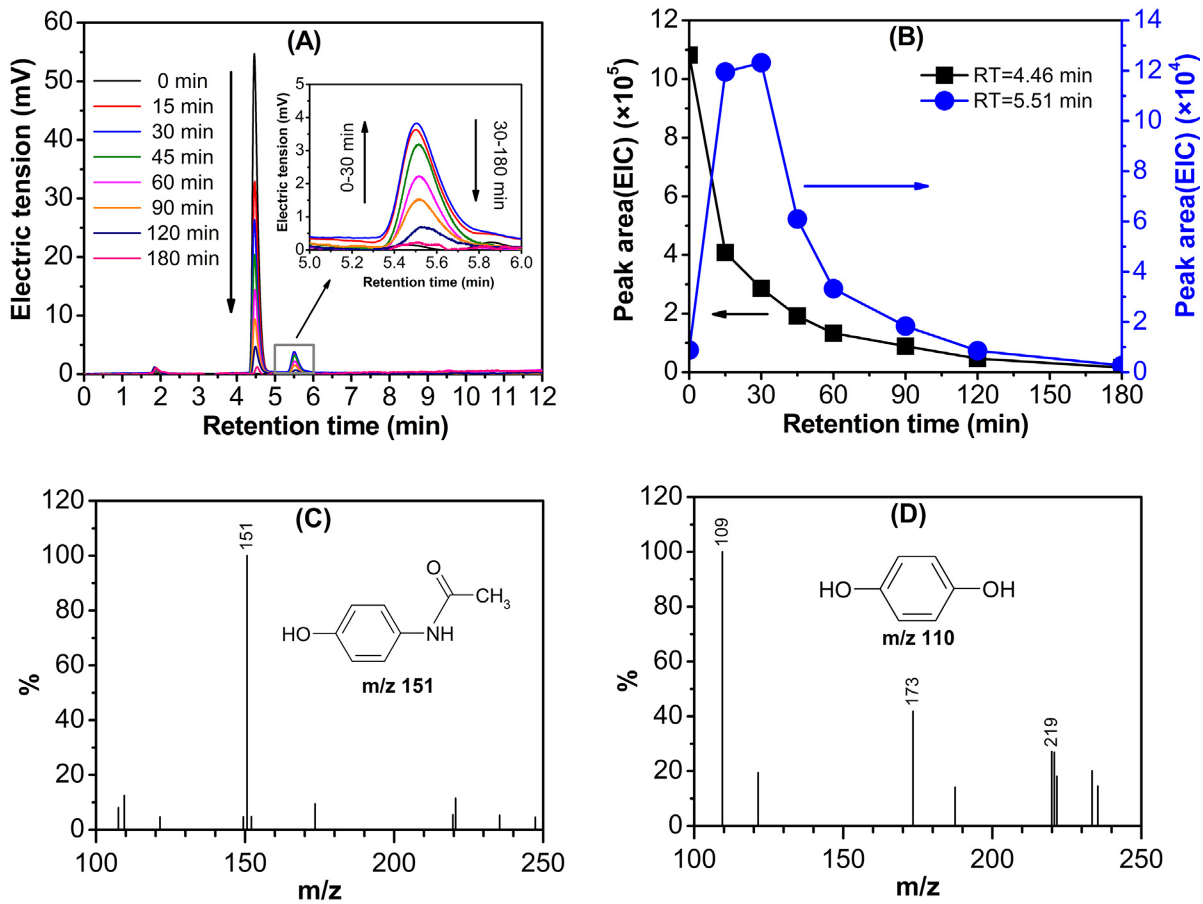

Fig. 7. (A) HPLC chromatograms of the APAP degradation over the as-synthesized β-Bi_2O_3 nanospheres under visible light irradiation; (B) evolution of the intermediates of the APAP degradation during the photocatalytic process calculated from the peak areas (in the extracted ion chromatogram (EIC)) of the product ions; (C and D) mass spectra and the corresponding proposed structures at retention times of 4.46 min and 5.51 min, respectively.

oxygen could trap the photogenerated electrons to form $^{\bullet}O_2^-$ radicals, which is beneficial to promote the decomposition of APAP. The result is consistent with previous reports that used bismuth-containing photocatalysts under visible light irradiation [59–61].

To further understand the photoreaction intermediate of APAP, a theoretical calculation of the frontier electron density of APAP was carried out, and the result is shown in Fig. 8B and Table 1. According to the frontier molecular orbital theory, for a radical reaction, the point of attack occurs at the position where the highest density of the sum of each electron occurs when they are in the highest occupied molecular orbital (HOMO) and lowest unoccupied molecular orbital (LUMO) [62], while for the direct hole oxidation, the first reaction site is predicted on the basis of $2FED^2_{HOMO}$ value [63]. In this study, the highest $2FED^2_{HOMO}$ value of APAP is found especially at the C_4 atoms (Table 1). Therefore, C_4 should be the first site from which an electron is extracted (Fig. 8B). The formed phenolic radical

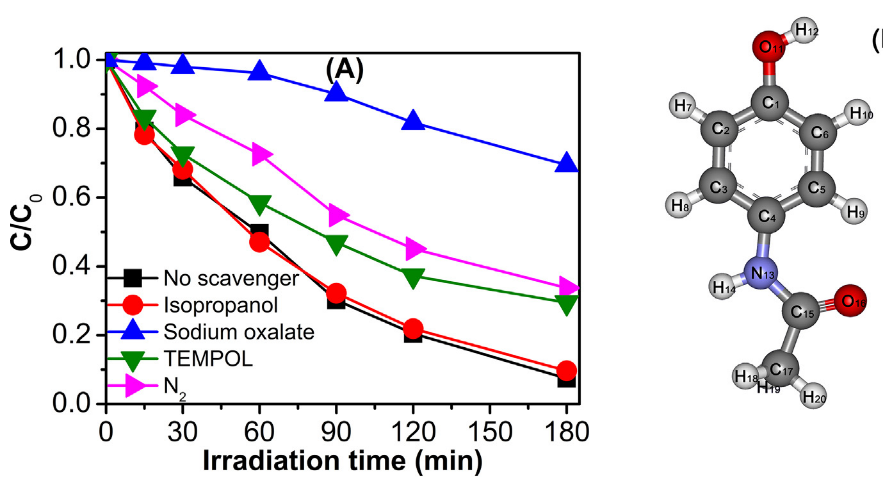

Fig. 8. (A) Photocatalytic degradation efficiency with different scavengers: no scavenger, 20 mmol L^{-1} isopropanol, 0.2 mmol L^{-1} sodium oxalate, 0.1 mmol L^{-1} TEMPOL, and N_2 in the photodegradation of APAP over as-synthesized β-Bi_2O_3 nanospheres; (B) the molecular structure of APAP with atoms labeled.

Table 1
The frontier electron density and atom point charge of APAP.

Atom label	$2FED^2_{HOMO}$	$FED^2_{HOMO} + FED^2_{LUMO}$
C_1	0.254	0.132
C_2	0.0968	0.366
C_3	0.0764	0.433
C_4	0.295	0.155
C_5	0.113	0.334
C_6	0.082	0.384
O_{11}	0.177	0.0897
N_{13}	0.259	0.13
C_{15}	0.00732	0.00467
O_{16}	0.0619	0.031
C_{17}	0.00198	0.00254

cation may be hydrolyzed to generate hydroquinone. Subsequently, the intermediate is further oxidized, resulting in the breakdown of aromatic structures followed by the formation of the carboxylate acid and carbon dioxide. Eventually, the APAP is mineralized into small inorganic molecules.

4. Conclusion

In summary, pure phase and monodisperse β-Bi_2O_3 nanospheres were successfully synthesized by a facile solvothermal–calcining process. XRD analysis and SEM observation of the samples obtained under various preparation conditions showed that the formation of β-Bi_2O_3 nanospheres went through a novel “in situ reduction” followed by an “in situ oxidation” route, in which the EG solvent, D-fructose, and calcining temperature play key roles. The as-synthesized β-Bi_2O_3 nanospheres exhibit strong photoabsorption in the UV and visible light region, with nanostructures and good dispersion, resulting in an excellent photocatalytic performance in the degradation of APAP under visible light irradiation. Because of the direct hole oxidation mechanism for the reaction of APAP and the high oxidation power of the synthetic β-Bi_2O_3 nanospheres, the intermediate products of APAP oxidation was relatively few, and a high mineralization efficiency was achieved. The β-Bi_2O_3 nanospheres synthesized by this facile method may have potential applications for water purification and can possibly be used in photovoltaic cells, photonic and optoelectronic devices, sensors, etc.

Acknowledgments

This work was financially supported by the Natural Science Foundation of Guangdong Province, PR China (Grant No. S2012040007074), the National Natural Science Foundation of PR China (Grant Nos. 21175047, 21071057, 20977036), and the research fund of the Key Laboratory of Fuel Cell Technology of Guangdong Province, PR China.

Appendix A. Supplementary data

Supplementary data associated with this article can be found, in the online version, at http://dx.doi.org/10.1016/j.apcatb.2013.04.037.

References

[1] C.G. Daughton, T.A. Ternes, Environmental Health Perspectives 107 (1999) 907–938.
[2] T.A. Ternes, A. Joss, H. Siegrist, Environmental Science and Technology 38 (2004) 392–399.
[3] P.M. Alvarez, J. Jaramillo, F. Lopez-Pinero, P.K. Plucinski, Applied Catalysis B: Environmental 100 (2010) 338–345.
[4] C. Su, A. Chang, L.M. Bellotindos, M. Lu, Separation and Purification Technology 99 (2012) 8–13.
[5] I. Quesada-Penate, C. Julcour-Lebigue, U.J. Jauregui-Haza, A.M. Wilhelm, H. Delmas, Journal of Hazardous Materials 221–222 (2012) 131–138.
[6] D. Lu, Y. Zhang, L. Wang, S. Lin, C. Wang, X. Chen, Talanta 88 (2012) 181–186.
[7] L.M.D.G. De, M.L. Veciana, C. Su, M. Lu, Journal of Hazardous Materials 217–218 (2012) 200–207.
[8] B. Habibi, M. Jahanbakhshi, M.H. Pournaghi-Azar, Electrochimica Acta 56 (2011) 2888–2894.
[9] B. Goezmen, Environmental Progress and Sustainable Energy 31 (2012) 296–305.
[10] A.S. Mestre, A.S. Bexiga, M. Proenca, M. Andrade, M.L. Pinto, I. Matos, I.M. Fonseca, A.P. Carvalho, Bioresource Technology 102 (2011) 8253–8260.
[11] J. Lu, Q. Huang, L. Mao, Environmental Science and Technology 43 (2009) 7062–7067.
[12] I. Kim, N. Yamashita, H. Tanaka, Chemosphere 77 (2009) 518–525.
[13] N. Klamerth, S. Malato, M.I. Maldonado, A. Aguera, A.R. Fernandez-Alba, Environmental Science and Technology 44 (2010) 1792–1798.
[14] I. Kim, H. Tanaka, Ozone: Science and Engineering 33 (2011) 150–157.
[15] I. Sires, J.A. Garrido, R.M. Rodriguez, P.L.L. Cabot, F. Centellas, C. Arias, E. Brillas, Journal of the Electrochemical Society 153 (2006) D1–D9.
[16] X. Zhang, F. Wu, X.W. Wu, P. Chen, N. Deng, Journal of Hazardous Materials 157 (2008) 300–307.
[17] L. Yang, L.E. Yu, M.B. Ray, Water Research 42 (2008) 3480–3488.
[18] N. Miranda-Garcia, S. Suarez, B. Sanchez, J.M. Coronado, S. Malato, M.I. Maldonado, Applied Catalysis B: Environmental 103 (2011) 294–301.
[19] M.R. Hoffmann, S.T. Martin, W.Y. Choi, D.W. Bahnemann, Chemical Reviews 95 (1995) 69–96.
[20] P. Xiong, J. Hu, Separation and Purification Technology 91 (2012) 89–95.
[21] L. Yang, L.E. Yu, M.B. Ray, Environmental Science and Technology 43 (2009) 460–465.
[22] C.A. Aguilar, C. Montalvo, J.G. Ceron, E. Moctezuma, International Journal of Environmental Research 5 (2011) 1071–1078.
[23] L. Huang, G. Li, T. Yan, J. Zheng, L. Li, New Journal of Chemistry 35 (2011) 197–203.
[24] L. Zhou, W.Z. Wang, H.L. Xu, S.M. Sun, M. Shang, Chemistry – A European Journal 15 (2009) 1776–1782.
[25] M. Muruganandham, R. Amutha, G.J. Lee, S.H. Hsieh, J.J. Wu, M. Sillanpaa, Journal of Physical Chemistry C 116 (2012) 12906–12915.
[26] S. Eda, M. Fujishima, H. Tada, Applied Catalysis B: Environmental 125 (2012) 288–293.
[27] C.Y. Wang, H. Zhang, F. Li, L.Y. Zhu, Environmental Science and Technology 44 (2010) 6843–6848.
[28] L.W. Zhang, T.G. Xu, X. Zhao, Y.F. Zhu, Applied Catalysis B: Environmental 98 (2010) 138–146.
[29] X.Q. Zhu, J.L. Zhang, F. Chen, Applied Catalysis B: Environmental 102 (2011) 316–322.
[30] Q.J. Ruan, W.D. Zhang, Journal of Physical Chemistry C 113 (2009) 4168–4173.
[31] G.K. Zhang, J.L. Yang, S.M. Zhang, Q. Xiong, B.B. Huang, J.T. Wang, W.Q. Gong, Journal of Hazardous Materials 172 (2009) 986–992.
[32] T. Kako, Z.G. Zou, M. Katagiri, J.H. Ye, Chemistry of Materials 19 (2007) 198–202.
[33] X. Xiao, C. Liu, R.P. Hu, X.X. Zuo, J.M. Nan, L.S. Li, L.S. Wang, Journal of Materials Chemistry 22 (2012) 22840–22843.
[34] X. Liu, H. Cao, J. Yin, Nano Research 4 (2011) 470–482.
[35] K. Brezesinski, R. Ostermann, P. Hartmann, J. Perlich, T. Brezesinski, Chemistry of Materials 22 (2010) 3079–3085.
[36] H. Jiang, K. Cheng, J. Lin, Physical Chemistry Chemical Physics 14 (2012) 12114–12121.
[37] H. Lu, S. Wang, L. Zhao, B. Dong, Z. Xu, J. Li, RSC Advances 2 (2012) 3374–3378.
[38] H. Cheng, B. Huang, J. Lu, Z. Wang, B. Xu, X. Qin, X. Zhang, Y. Dai, Physical Chemistry Chemical Physics 12 (2010) 15468–15475.
[39] G. Yang, Z. Jiang, H. Shi, T. Xiao, Z. Yan, Journal of Materials Chemistry 20 (2010) 5301–5309.
[40] S. Panigrahi, S. Kundu, S. Ghosh, S. Nath, T. Pal, Journal of Nanoparticle Research 6 (2004) 411–414.
[41] Y. Sun, Y. Xia, Science 298 (2002) 2176–2179.
[42] X. Xiao, W.D. Zhang, RSC Advances 1 (2011) 1099–1105.
[43] A. Bagno, M. Genovese, A. Luchini, M. Dettin, M.T. Conconi, A.M. Menti, P.P. Parnigotto, C. Di Bello, Biomaterials 25 (2004) 2437–2445.
[44] M. Gui, W. Zhang, Journal of Physics and Chemistry of Solids 73 (2012) 1342–1349.
[45] P.J. Sadler, H. Li, H. Sun, Coordination Chemistry Reviews 185–186 (1999) 689–709.
[46] Y. Wang, S. Li, X. Xing, F. Huang, Y. Shen, A. Xie, X. Wang, J. Zhang, Chemistry – A European Journal 17 (2011) 4802–4808.
[47] J. Chen, S. Qin, Y. Liu, F. Xin, X. Yin, Research on Chemical Intermediates (2013) 1–12.
[48] X. Jiang, Y. Wang, T. Herricks, Y. Xia, Journal of Materials Chemistry 14 (2004) 695–703.
[49] G. Zhang, M. Liu, Journal of Materials Science 34 (1999) 3213–3219.
[50] S.J. Lee, C.H. Lee, Materials Letters 56 (2002) 705–708.
[51] J.W. Tang, Z.G. Zou, J.H. Ye, Angewandte Chemie International Edition 43 (2004) 4463–4466.
[52] X. Zhang, Z.H. Ai, F.L. Jia, L.Z. Zhang, Journal of Physical Chemistry C 112 (2008) 747–753.

[53] F. Qin, G. Li, R. Wang, J. Wu, H. Sun, R. Chen, Chemistry – A European Journal 18 (2012) 16491–16497.
[54] Y. Xu, M.A.A. Schoonen, American Mineralogist 85 (2000) 543–556.
[55] J. Xu, W. Meng, Y. Zhang, L. Li, C. Guo, Applied Catalysis B: Environmental 107 (2011) 355–362.
[56] N.M. Mahmoodi, M. Arami, N.Y. Limaee, Journal of Hazardous Materials 133 (2006) 113–118.
[57] W. Wang, T.W. Ng, W.K. Ho, J. Huang, S. Liang, T. An, G. Li, J.C. Yu, P.K. Wong, Applied Catalysis B: Environmental 129 (2013) 482–490.
[58] W. Wang, Y. Yu, T. An, G. Li, H.Y. Yip, J.C. Yu, P.K. Wong, Environmental Science and Technology 46 (2012) 4599–4606.
[59] C. Wang, L. Zhu, C. Song, G. Shan, P. Chen, Applied Catalysis B: Environmental 105 (2011) 229–236.
[60] Y. Li, J. Wang, H. Yao, L. Dang, Z. Li, Journal of Molecular Catalysis A: Chemical 334 (2011) 116–122.
[61] R. Hao, X. Xiao, X. Zuo, J. Nan, W. Zhang, Journal of Hazardous Materials 209–210 (2012) 137–145.
[62] N. San, A. Hatipoğlu, G. Koçtürk, Z. Çınar, Journal of Photochemistry and Photobiology A: Chemistry 146 (2002) 189–197.
[63] K. Fukui, T. Yonezawa, H. Shingu, Journal of Chemical Physics 20 (1952) 722–725.